Research Article Vol. 62, No. 19 / 1 July 2023 / Applied Optics 5139

applied optics

Spectral and RGB analysis of the light climate and its ecological impacts using an all-sky camera system in the Arctic

Stephen Grant,[1,*] Geir Johnsen,[1,2] David McKee,[3,4] Artur Zolich,[1] and Jonathan H. Cohen[5]

[1]Centre for Autonomous Marine Operations and Systems, Department of Biology, Norwegian University of Science and Technology (NTNU), Trondheim Biological Station, NO-7491 Trondheim, Norway
[2]University Centre in Svalbard (UNIS), P.O. Box 156, NO-9171 Longyearbyen, Norway
[3]Department of Physics, University of Strathclyde, Glasgow G4 0NG, Scotland, UK
[4]Faculty of Biosciences, Fisheries and Economics, UiT The Arctic University of Norway, NO-9037, Tromsø, Norway
[5]School of Marine Science & Policy, University of Delaware, 700 Pilottown Rd., Lewes, Delaware 19958, USA
*stephen.grant@ntnu.no

Received 7 December 2022; revised 5 March 2023; accepted 22 March 2023; posted 22 March 2023; published 21 June 2023

The ArcLight observatory provides an hourly continuous time series of all-sky images providing light climate data (intensity, spectral composition, and photoperiod) from the Arctic (Svalbard at 79°N). Until recently, no complete annual time series of light climate relevant for biological processes has been provided from the high Arctic because of insufficient sensitivity of commercial light sensors during the Polar Night. The ArcLight set up is unique, as it provides both all-sky images and the corresponding integrated spectral irradiance in the visible part of the solar electromagnetic spectrum (E_{PAR}). Here we present a further development providing hourly diel-annual dynamics from 2020 of the irradiance partitioned into the red, green, and blue parts of the solar spectrum and illustrate their relation to weather conditions, and sun and moon trajectories. We show that there is variation between the RGB proportions of irradiance throughout the year, with the blue part of the spectrum showing the greatest variation, which is dependent on weather conditions (i.e., cloud cover). We further provide an example of the biological impact of these spectral variations in the light climate using *in vivo* Chl a-specific absorption coefficients of diatoms (mean of six low light acclimated northern-Arctic bloom-forming species) to model total algal light absorption (AQ_{total}) and the corresponding fraction of quanta used by Photosystem II (AQ_{PSII}) (O_2 production) in RGB bands and the potential impacts on the photoreceptor response, suggesting periods where repair and maintenance functions dominate activity in the absence of appreciable levels of red or green light. The method used here can be applied to light climate data and spectral response data worldwide to give localized ecological models of AQ.

https://doi.org/10.1364/AO.480454

1. INTRODUCTION

The Polar Night period experienced in Arctic regions has long been thought to be a period of reduced ecological activity [1]. However, this perception has been challenged in recent years, and it is now known that the ecosystem is fully active during this period, with light levels playing a major role as a cue for biological processes [2–5]. With improved monitoring of the Arctic light climate (E_{PAR}, $E(\lambda)$, and photoperiod) as a motivation, the ArcLight light observatory (located at Ny-Ålesund, Svalbard, 79°N) (Fig. 1) was established to provide light climate measurements throughout the year as part of the "Applied technology, biological interactions and consequences in an era of abrupt climate change" infrastructure project funded by the Norwegian Research Council. The observatory is a small hut containing several light sensors. It was first established in 2016 and has been continuously collecting data since January 2017. The main sensors of interest in this context are an USSIMO hyperspectral spectroradiometer (providing spectral irradiance in the visible region) and a Canon 5D Mark III camera with a fisheye lens providing an estimate of the spectrally integrated downwelling irradiance from the camera derived luminance in the visible range (400–700 nm, or photosynthetic active radiation, denoted E_{PAR}) and all-sky images, respectively. All measurements are taken at a 180° viewing angle pointing towards the zenith.

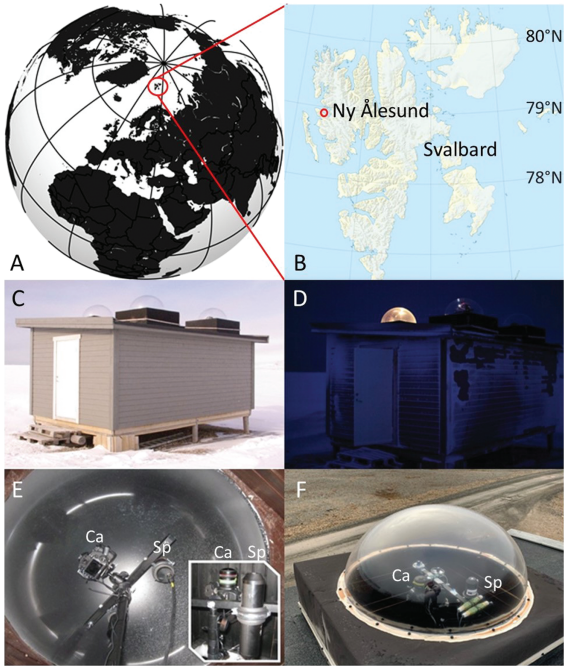

Fig. 1. A, location of Svalbard (red circle). B, position of the ArcLight light observatory west of Ny-Ålesund (red circle) in Kongsfjorden, Spitsbergen (major island of the Svalbard archipelago). C, outside of the Arclight hut. D, during the Polar Night with one of four domes illuminated for illustration purposes. E, camera (Ca) and spectroradiometer (Sp) with apertures pointing upwards through a plexiglass dome. The inset shows the all-sky camera and spectroradiometer. F, sensors viewed from outside the dome.

The observatory offers a unique environment in which to study the light climate and its biological or ecological impacts. Although at this latitude there are extended periods when the sun remains below (Polar Night) or above (Midnight Sun) the horizon during the entire diel cycle [6], the light climate is dynamic and shows great variation in intensity and spectral composition over both the (diel) 24-h and annual cycle. There are also additional contributors to the light climate, including lunar illumination and the *aurora borealis* [1,3,7–11].

The light climate can be considered to consist of three components: total visible irradiance, E_{PAR}; spectral irradiance, $E(\lambda)$; and photoperiod [12]. These three aspects act as a cue for light-mediated processes of all organisms, and documenting them in detail is relevant for understanding and modeling many biological phenomena such as phytoplankton blooms and light-induced effects on microbes, terrestrial plants, invertebrates, fish, birds, and mammals, in both air and water. Previous publications [3–5,7–11] have shown that, even during the long dark winter periods, light remains the major cue for biological processes, and there is sustained activity of the ecosystem throughout what was once believed to be a dormant period for the region.

A year-round time series of light climate data from the Arctic, with a focus on the Polar Night, was previously presented in [13], including a long-term (four-year) time series of irradiance measurements showing in detail high diel variation of E_{PAR} across seasons, even during the dark winter periods when the moon is the chief illumination source [9,10]. With respect to further investigation of biologically relevant features and applications using time-series data of light climate from this region, this paper acts as a companion to [13]. The salient feature of the all-sky camera is its sensitivity range which far exceeds the majority of commercially available spectroradiometers and dedicated (PAR) sensors. Previously we have shown that it was possible to cross-calibrate the camera images to PAR measurements from a spectroradiometer (USSIMO) to establish camera-based E_{PAR} measurements, and then to extrapolate the calibration to allow measurement of E_{PAR} during periods of Polar Night "darkness" when the light levels were below the detection limits for other sensors. Consequently, as data derived from the camera are not fully spectrally resolved, they do not provide some of the nuances of the other observatory measurements, particularly when compared to the spectrally resolved spectroradiometer data. Of course, the camera naturally records images using three spectral bands (RGB), and here we explore the potential to go beyond E_{PAR}, moving towards estimation of $E(\lambda)$ in three broad spectral bands corresponding to the RGB properties of the camera.

The focus of this paper is on the further use of the light climate data collected by the ArcLight observatory, rather than the collection methods themselves, focusing on the spectral composition of incident light and its interaction with organismal photoreceptors throughout the year. The objective is to look at the spectral composition of the data acquired with the camera, with particular focus on the ecologically relevant visible range from 400 to 700 nm. Additionally, we investigate changes in the broadband spectral composition throughout the year to determine RGB wavebands that are dominant at different times of year, temporal differences that can be observed, and how this information can be of ecological significance. As different photoreceptors respond to different wavelengths, or wavebands, of light [14], we can potentially identify periods of the year which facilitate different gene expression and organismal responses based on the spectral composition of the available light.

A step-by-step procedure for handling both spectroradiometer and camera data is presented. The time-series data presented here were collected between January and December 2020 to illustrate the light climate dynamics through an annual cycle. However, some additional examples from earlier times are also used.

2. MATERIALS AND METHODS

A. Spectroradiometer

The USSIMO spectroradiometer is a hyperspectral planar irradiance meter (In-situ Marine Optics, Perth, WA, Australia) equipped with a Zeiss MMS1 UV-VIS NIR detector and National Institute of Standards and Technology (U.S.) traceable radiometric calibration between 380 and 900 nm. This instrument is used for time-series measurement of the downwelling spectral irradiance in energy ($\mathrm{W\,m^{-2}\,nm^{-1}}$) or quanta [$\mu\mathrm{mol\ quanta\,m^{-2}\,s^{-1}\,nm^{-1}}$] units for the comparison and verification of E_{PAR} derived from the camera. Spectral resolution is 10 nm (3.3 nm pixel spacing), and a cosine-corrected polytetrafluoroethylene light diffusor of a 180° viewing angle with a cosine error of <3% (0–60°), <10% (60°–87.5°) is fitted. The detection limit for the spectroradiometer is E_{PAR} of

0.016 W m^{-2} [13], providing useable data from mid-February to mid-November. The device acquired measurements with a 16 bit analog-to-digital converter, with a sampling rate up to 5 Hz and integration time from 1 to 6000 ms. This sensor is equipped with additional GPS, pitch, roll, heading, internal temperature, and depth sensors. The pitch and roll sensor is used to ensure that the spectroradiometer remains in a fixed position throughout the time-series acquisition. In this work, we are specifically looking at the irradiance in the PAR range of 400–700 nm.

B. Camera

The all-sky camera is a Canon 5D Mark III EOS camera (Canon Inc., Tokyo, Japan) with a full-size CMOS sensor (36 × 24 mm, providing a crop factor of 1) and with 22.3 mega-pixel effective spatial resolution. For a detailed description, see [13]. The camera is equipped with a fish-eye lens (Canon EF 8-15 mm f/4L) with a focal length set to 8 mm and with the aperture manually set to open (f/4) to ensure maximum light sensitivity, providing a 180° image of the atmosphere. Both shutter speed (ranging from 0.000125 to 30 s) and ISO (light gain sensitivity, ranging from 100 during the Midnight Sun period and 6400 during the Polar Night) are variable to obtain correct light exposure. The camera system is calibrated to provide E_{PAR} in W m^{-2} by using data from the red, green, and blue wavebands (RGB channels) for postprocessing. The camera is controlled using Canon EOS Utility software and a custom script to acquire images at user specified times (note all times are in UTC). Pictures acquired in RAW format are saved in JPEG file format with quality: 97, subsampling ON (2 × 1). The white balance was manually set to "daylight." The spatial resolution of each image is 5760 × 3840 pixels with a 24 bit per pixel color depth, distributed with 8 bits for each channel of red, green, and blue, giving an sRGB color space of the pictures according to the IEC standard specifications [13]. All files are marked with an additional metadata information set. The conversion of RGB images to E_{PAR} is described in detail in section 2.3 of [13].

One of the main benefits of using a camera system is that RGB channel data are readily available. This allows for simple extraction of RGB information using an adaptation of the method outlined in [1] applied to individual color channels to obtain a time series for red, green, or blue light (wavebands outlined in section 2.4, Fig. 5) over the full 2020 annual cycle period.

C. Masking

The ArcLight observatory is situated in a remote location, but is within the line of sight of the Ny-Ålesund settlement. All-sky images recorded at the site include artificial light sources near the horizon at fixed positions (streetlights and airport lights) that need to be masked out in the first stage of image processing. This was not carried out in [13], but was found to be significant when analyzing the spectral composition of the light, particularly in the red color channel. This is handled during postprocessing of the images where, prior to irradiance calculations, a binary mask is applied (Fig. 2). The mask is designed to remove the majority of the lights from the settlement (shown in Fig. 2(A)). Some of the other visible lights are transient lights from vehicles or other sources and thus are not masked.

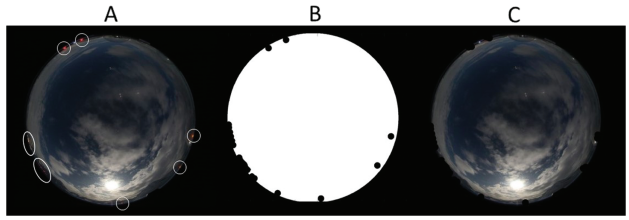

Fig. 2. A, example of an all-sky image with circles indicating artificial light sources. B, binary mask applied. C, resulting "masked" image.

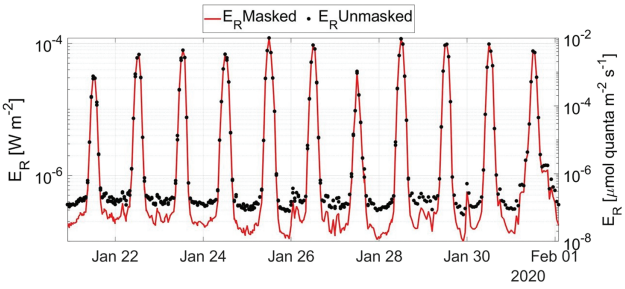

Fig. 3. Black circles represent the unmasked red channel downwelling irradiance (E_R) with artificial lights present; the red line shows the same dataset after masking to remove artificial light sources. Note that the Y axes are in log-scale.

Figure 3 shows the difference in calculated E_R (irradiance for the red waveband method outlined below) during January 2020 for masked and unmasked images. When masking is carried out, the effect of direct illumination from artificial light sources is accounted for at the darkest point of the night, leading to a reduction in the irradiance measured in the red channel at these times without affecting the irradiance at other times. The effect of skyglow from artificial sources will still be present despite masking.

The $E(\lambda)$ measured is highly variable based on weather conditions and the movement or appearance of temporary artificial light sources. However, selecting only dark nights (those without the moon visible) between the hours of 23:00 and 01:00 in selected periods (January 21–February 1, February 20 to March 1, October 10–20, November 10–20, December 10–20) allows for some quantification of the average reduction in artificial light seen following masking. For the downwelling irradiance, in all channels (E_{PAR}) there was an average reduction of 24% with a standard deviation of ±8%, but this varies across the color channels with the red channel (E_R) seeing the largest reduction after masking, corresponding to the large number of red artificial lights in the settlement. The irradiance in each channel on clear moonless nights was reduced by an average of $-40 \pm 14\%$, red channel; $-16 \pm 6\%$, green channel; and $-22 \pm 13\%$, blue channel. The ability to postprocess images and mask/target specific regions of an image is an additional benefit of using the all-sky camera as a light sensor.

D. RGB Camera Data Adjustment

This section outlines the adaptations needed to the method outlined in [13] to accommodate RGB processing. Starting from the calculation of the relative luminance (Eq 4. In [13]), a separate relative luminance is calculated for each color channel (represented by subscript X, i.e., for the red color channel, the relative luminance is Y_R) for both the light and dark regions, where w_X is the color channel specific weighting function ($w_R - 0.2126$, $w_G - 0.7152$, $w_B - 0.0722$) [15] to convert the sRGB values to the relative luminance:

$$Y_X = w_X \cdot \overline{X_s}. \quad (1)$$

The chief difference between methods here and in [13] is that in Eq. (1) (related to Eq. (4) in [1]) we calculate Y_X for each channel without recombining them into a total Y value, as shown schematically in Fig. 4.

This relative luminance value, Y_X, is then corrected for both dark current and the various camera settings, including exposure time (t), aperture (N), and ISO (S), in line with a number of key assumptions (e.g., the aperture is kept constantly open to ensure maximum light penetration; the pixel values change linearly with changing ISO and exposure times, and the absolute luminance is linearly proportional to E_{PAR}) as detailed and verified in [13,16,17]:

$$Y_X\text{corr} = Y_X\text{Light} - Y_X\text{Dark}, \quad (2)$$

where $Y_X\text{Light} = Y_X(N^2/St)$ for the light region, and $Y_{X\text{Dark}} = Y_X(N^2/St)$ for the dark region.

Finally, Eq. (3) converts from $Y_X$corr to E_X using a color band specific scaling variable, j_X. This is derived from a comparison between the camera derived irradiance and the irradiance as measured using the spectroradiometer, calibrated for the absolute irradiance, during a period where the light levels are above the threshold of the spectroradiometer. The spectral response bands of the camera (R: 505–691 nm, G: 468–635 nm, and B: 412–555 nm) [18] were applied to the spectroradiometer data to obtain comparable irradiance data:

$$E_X \approx Y_X\text{corr} \cdot j_X. \quad (3)$$

An explanation of this j_X term is included in [13] and it is obtained by minimizing the "Mean Average Percentage Error" (MAPE) using the following equation:

$$\text{MAPE} = \frac{100\%}{n} \sum_{i=1}^{n} \left| \frac{E_X\text{Spec} - Y_X\text{corr} \cdot j_X}{E_X\text{Spec}} \right|. \quad (4)$$

As described in [13], minimizing the mean average percentage error (MAPE) will allow us to use this spectroradiometer data to verify and adjust the camera E_X data to more accurately reflect the RGB proportions as measured using the spectroradiometer (E_XSpec). By applying Eq. (4) to the time synchronized spectroradiometer and camera data, the color channel specific adjustment value, j_X, was determined as $j_R = 1.6163$, $j_G = 0.4804$, and $j_B = 2.9296$ for each channel. The j-adjusted camera data can then be used to produce a time series of proportions of RGB irradiance throughout the year, including during the low light Polar Night periods.

To allow a comparison between the spectroradiometer and camera derived irradiance values, the wavelength bands corresponding to the spectral sensitivity of the camera [18] (Fig. 5(A)) can be applied to the spectroradiometer data allowing for calculation of a spectroradiometer derived irradiance in each color channel (E_XSpec). Figure 5(B) shows the $E(\lambda)$ measured on June 21, 2020, at noon with the colored arrows indicating the bands applied based on the camera spectral response. Figure 5(C) shows the E_XSpec values calculated across the entire 400–700 nm range and within each color band. Due to the

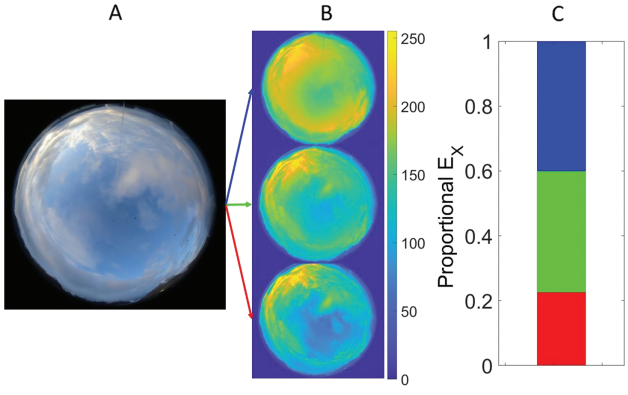

Fig. 4. Schematic of the process from A, initial image, through B, division into constituent color channels. B also indicates the intensity scale for the RGB values. C, stacked bar representing the proportion of the total calculated E_{PAR} per channel.

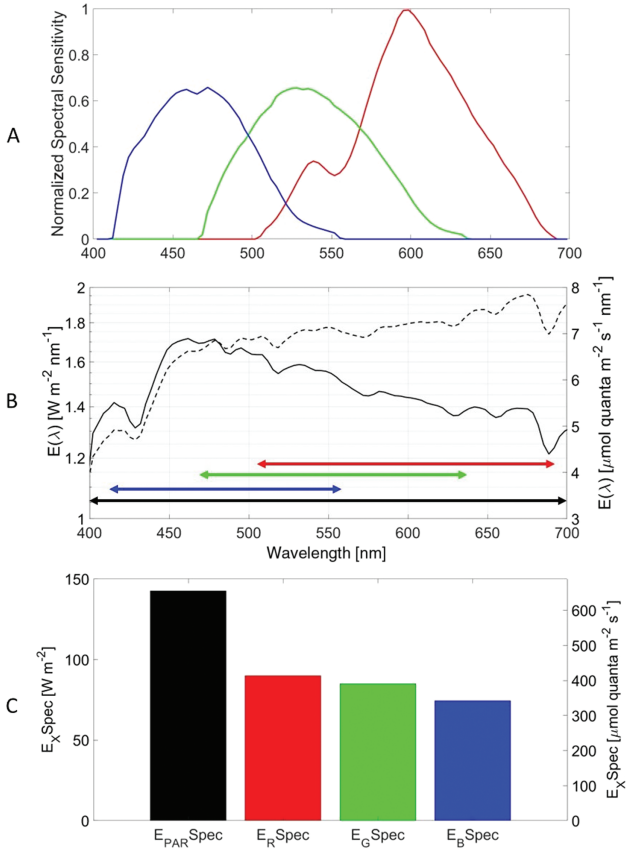

Fig. 5. A, spectral response of the Canon camera CMOS sensor. B, $E(\lambda)$ measured at noon on June 21, 2020, with arrows representing spectral bands applied based on A with the $E(\lambda)$ spectrum in both energy (solid line) and quanta (dashed line) units. C, calculated E_XSpec values for the PAR range and individual color (RGB) channels.

overlap of the spectral response bands, the E_{PAR}Spec value is less than the sum of the individual color channels (E_XSpec).

E. Absorbed Quanta for Photosynthesis Calculation

As noted in [19] and shown in Eq. (5), absorbed quanta (AQ) of a given photosynthetic organism depends on the spectral composition of the ambient light, $E(\lambda)$, and the corresponding spectral *in vivo* Chl a-specific absorption coefficients of the organism, $A(\lambda)$, detailed below in Eq. (5). An estimate for AQ at a given wavelength can be calculated using $E(\lambda)$ in either individual wavelength intervals or wavebands. Using wavebands, the camera data can also be used to provide an insight into AQ during the Polar Night:

$$\mathrm{AQ}_{\mathrm{total}} \text{ or } \mathrm{AQ}_{\mathrm{PSII}} = \left[\int_{\lambda\,\mathrm{min}}^{\lambda\mathrm{max}} A(\lambda)\cdot E(\lambda)\mathrm{d}\lambda\right], \qquad (5)$$

where AQ_{total} (μmol quanta (mg Chl a)$^{-1}$ s^{-1}) is the rate of quanta absorption per unit mass of Chl a as an indication of biomass (for both light harvesting and photoprotective pigments); $\mathrm{AQ}_{\mathrm{PSII}}$ is the corresponding AQ transported to PSII (utilized quanta for oxygenic photosynthesis); and $A(\lambda)$ is either $a^*_{\varphi}(\lambda)$, the *in vivo* spectral Chl a specific light absorption coefficient per nm, or $F^*_{\mathrm{PSII}}(\lambda)$, the *in vivo* spectral light utilized by PSII per nm (by means of PSII scaled *in vivo* fluorescence excitation spectra), as detailed in Johnsen and Sakshaug [19]. $E(\lambda)$ is the *in situ* spectral irradiance, and λ_{min} and λ_{max} are the boundaries of the waveband being investigated. Note that the light measurements in this work are of light incident on the sea surface; therefore, the irradiance values here represent the maximum irradiance that an organism in the upper layers of the water would be exposed to. Care must be taken to extrapolate our light climate measurements in air providing absolute maximum E values at the surface to underwater conditions, for example, at a 1 m depth, the irradiance would be reduced by, on average, ∼33%, as determined by the HEIMDALL spectral light field model [20].

3. RESULTS

A. Spectroradiometer

Using the spectroradiometer we can look at the spectral irradiance in the E_{PAR} range captured at each point in the time series. For this work, data from 2020 is used, as this year has the most complete dataset for both the camera and the spectroradiometer. The data are presented in both W m^{-2} nm^{-1} and μmol quanta m^{-2} s^{-1} nm^{-1} using the conversion outlined in ([21], Appendix A, "Units," p. 569).

Figure 6 shows a representative all-sky downwelling irradiance spectrum, $E(\lambda)$, acquired on June 10, 2020, at 12:56. This shows the spectral irradiance measured by the spectroradiometer. We can see here that, at this time, blue wavelengths dominated in terms of energy, and a peak energy typical of sunlight was seen at ∼460 nm. This spectrum is typical of a clear blue sky, exhibiting the blue light of Rayleigh scattering from water vapor, ozone, dust, and other particulates in the atmosphere.

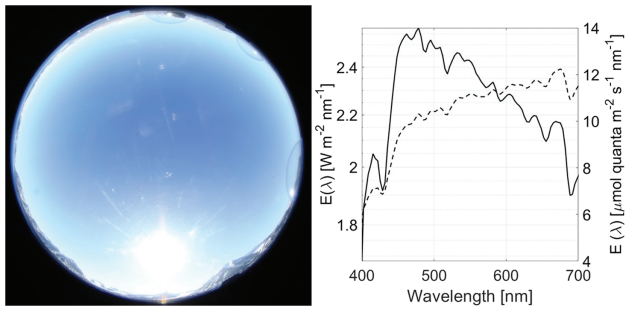

Fig. 6. All-sky image from June 10, 2020, and the corresponding USSIMO $E(\lambda)$ spectrum in both energy (solid line, primary Y axis) and quanta (dashed line, secondary Y axis) units.

To investigate how this pattern changes over time we can look at dates of interest. In the first instance, we will look at the solstices and equinoxes in 2020, providing the extremes in annual light climate in the Arctic. Figure 7 shows $E(\lambda)$ from March 20 at 04:58, June 20 at 23:55, September 22 15:59, and December 21 at 11:00. These times were as close as possible to timings of the spring equinox, summer solstice, autumn equinox, and winter solstice in Ny-Ålesund, respectively. There is a clear difference in $E(\lambda)$ at the equinoxes and solstices. However, the shapes of the spectra for all but the winter solstice are relatively constant when displayed on a logarithmic scale. The green line (Dec. 21) is effectively the dark signal. Models such as HEIMDALL [20] predict a spectral irradiance level of 10^{-8} Wm^{-2} nm^{-1} for the winter solstice, as shown in Fig. 3 of that paper. This is below the detection threshold of the USSIMO spectroradiometer. This highlights one of the limitations of the spectroradiometer to acquire measurements in low light conditions: the all-sky images show streetlights and other light sources visible in the dark periods, but they are not detected by the spectroradiometer. As shown in Fig. 3, these lights have a measurable impact on the E_X detected by the camera. This is partly explained by the difference in optical configuration with the camera fish-eye lens being much more sensitive to light arriving horizontally than the spectroradiometer's cosine collector which is designed to have a zero response to horizontal incoming light.

Apart from looking at specific times of year, we can also look at particular environmental conditions. Figure 8 shows a comparison between different sun angles of +1° and −2° with images taken 1 h apart on October 6, 2020. Both are low light scenarios with an order of magnitude between them; however, the shape of the spectra shows a peak in the red wavelengths once the sun is below the horizon. This is largely dependent on the sun angle; the lower angle leads to increased scattering, preferentially in blue wavelengths, as the optical path for solar radiation is increased, but clouds are seen to reflect red light particularly well under these conditions.

Calculating the E_XSpec for each time point in the time series gives us an annual time series of E_XSpec values. Figure 9(A) shows the E_XSpec measurements from the USSIMO spectroradiometer for 2020 for the three defined wavebands. The gray horizontal line again represents a detection limit for a spectroradiometer which here is used to filter data. Note that only the noon and midnight values are shown in time-series plots

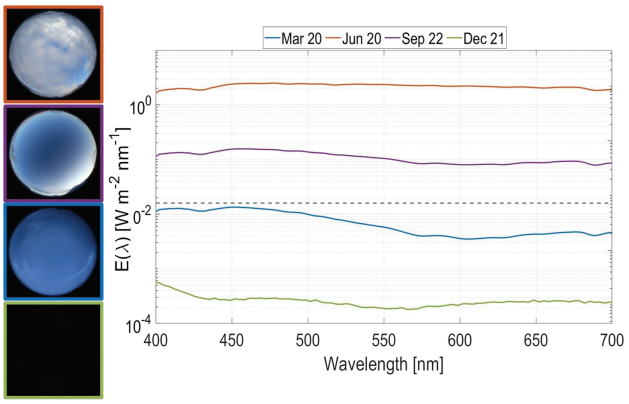

Fig. 7. $E(\lambda)$ spectra measured with the USSIMO spectroradiometer on four dates: the spring equinox March 20, the summer solstice June 21, the autumn equinox September 23, and the winter solstice December 22. The dashed gray line shows the detection threshold of the spectroradiometer (Note: this detection limit is an E_{PAR} limit used for thresholding of data. This limit is a broadband value for the entire PAR range, a spectrally resolved detection limit was not available and, as such, the dashed gray line indicates a level below which data become less reliable, but are not necessarily simply noise.)

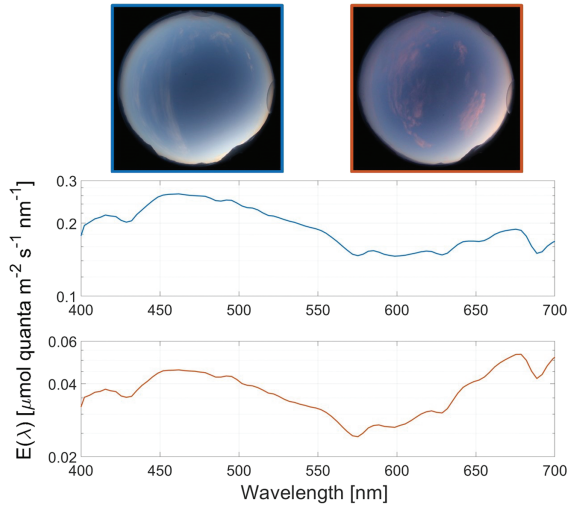

Fig. 8. Comparison of $E(\lambda)$ for different environmental conditions; first image (upper left) taken when the sun was 1° above the horizon (blue, October 6, 2020, 14:59 UTC) and the second (upper right) taken 1 h later with the sun having set and the sun angle being −2° (orange, October 6, 2020, 15:59 UTC) illustrating higher levels of red light due to atmospheric scattering present once the sun is below the horizon.

for clarity's sake, with the noon values highlighted with blue shading and the midnight values highlighted with red shading. The background region shading corresponds to the Polar Night (gray, December–February) and Midnight Sun (yellow, April–August) periods as defined in [13]; the red and green lines indicate the equinox and solstice dates, respectively. This color scheme is continued in subsequent plots. Figure 9(B) shows the proportion of E_XSpec in each color channel throughout the year calculated as a percentage of the total measured irradiance contributed by each waveband. The black areas of the plot are

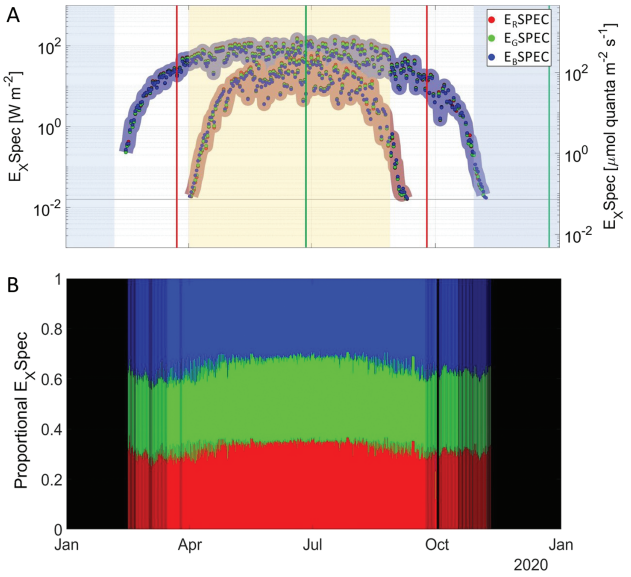

Fig. 9. A, spectroradiometer derived irradiance in RGB wavebands (E_XSpec). Upper curve E_{RGB} at noon (blue shading) and lower curve E_{RGB} at midnight (red shading). B, normalized irradiance proportions. The low light periods (below applied threshold) are removed. The blue and yellow background shaded areas denote the Polar Night and the Midnight Sun periods, while the red lines denote the equinox, and the green lines denote solstices.

areas falling below our applied threshold. These low light conditions can be overcome using the camera data in a similar manner to [13].

B. Camera

Carrying out the calculations outlined above also allows for the creation of an annual RGB time series from the camera data. Figure 10(A) shows a time series from January 1, 2020 to December 31, 2020, which illustrates the dynamic nature of the spectral composition of the light climate in the low light periods which was not detected by the spectroradiometer. During autumn, a diel period of ∼24 h ceases, with changes in the light level during the low light periods principally driven by the lunar cycle of full moons, seen as an intensity increase across all wavebands. Red light is seen to be much more prominent in the summer and winter months, and blue light dominates during the transitional spring and autumn periods (Fig. 10(B)). The prominence of red light during the darker winter periods is greatly affected by artificial light at night (ALAN); even with masking that removes direct light, there is significant skyglow from artificial sources affecting the spectral composition. In February/March and August–October (Fig. 10(C)), the daily change from a red hue being the dominant color at night to blue being the largest during the day that can be seen. A wavelet analysis, using the WaveletComp package in R [22], carried out in the autumn identified a ∼24 h period which stops at the end of September, (when the lunar cycle starts to dominate), indicating the transition from a diel cycle to a longer lunar period. This aligns with ecologically significant periods of change in the life cycle of phytoplankton and higher plants.

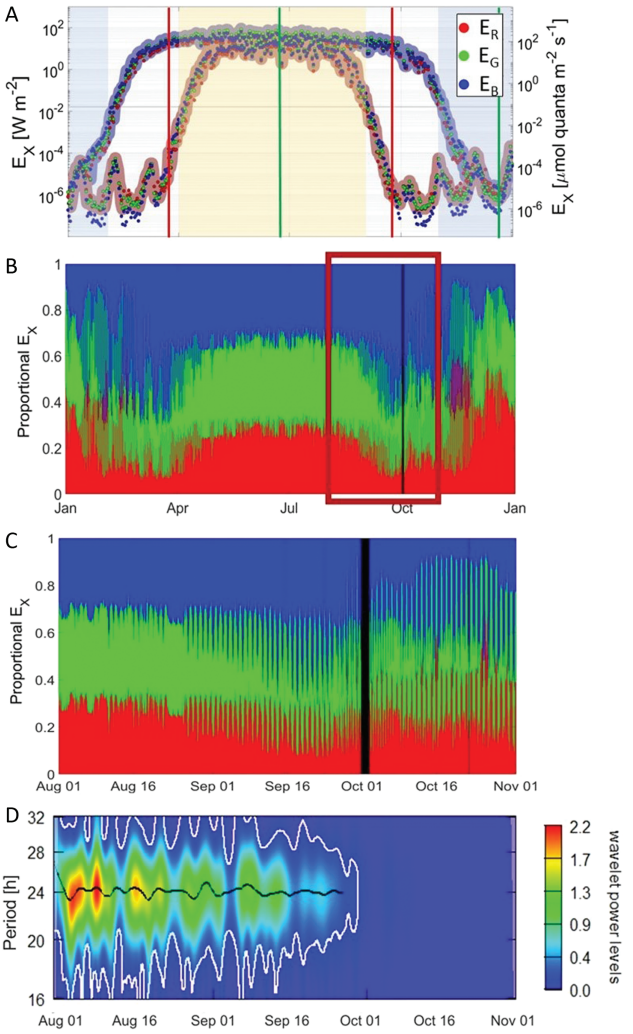

Fig. 10. A, E_X from the all-sky camera for each color channel across the year. Unlike the spectroradiometer data, detailed information about the light climate in the low light periods of the Polar Night can be detected. The blue and yellow shaded areas denote the Polar Night and the Midnight Sun periods, while the red lines denote the equinox, and the green lines denote solstices. B, Color channel proportions throughout 2020. C, color channel proportions for August to October 2020. D, wavelet analysis showing a 24h period ending in September; the black line represents the dominant period, with the white lines delineating significance boundaries for the period estimate (alpha = 0.05).

4. APPLICATIONS AND DISCUSSION

Figure 11 shows the all-sky photographs associated with the maximum proportion of each color band for the 2020 annual cycle. For example, the largest proportion of red irradiance found during the whole year was observed during the Polar Night on February 20, 2020, at 02:58:59, when there was cloud cover reflecting light pollution, mostly due to sodium streetlamps producing an orange hue from the nearby settlement. Note that due to the masking, the direct illumination from the streetlights themselves was not included in the calculation. The largest green proportion coincided with the aurora being

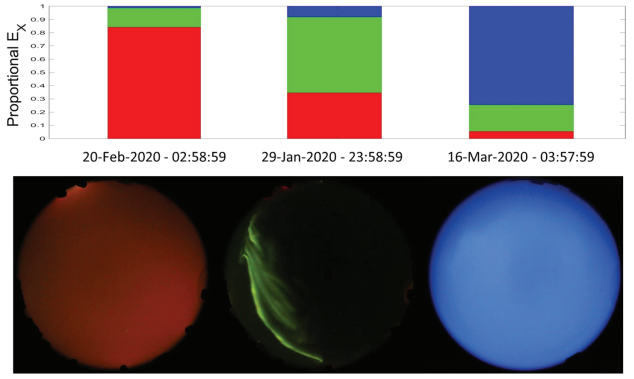

Fig. 11. Example of all-sky images showing light pollution, the aurora borealis, and an overcast spring night. The bar chart shows the relative proportions of the RGB channels.

active at January 29, 2020, at 23:58:59. The largest blue proportion occurred on a cloudy March night on March 16, 2020, at 03:57:59 at the onset of the Midnight Sun period.

Using this method, we can select for days with light pollution in the form of ALAN (heavily affected by reflected light from low altitude cloud cover at a height of approximately 500 m) or aurora by searching for the highest proportion of the total light in the relevant color channel. Both environmental factors have been shown to be ecologically important and are widely studied [1,3,7,8,23].

Light pollution, in this instance defined as periods when the red channel irradiance accounted for more than 50% of the total irradiance (highest proportion of red observed was 84%), was detected by this method to occur at 890 time points in the time series, though less significant light pollution (E_R greater than both E_G and E_B, but less than 50%) occurred throughout the periods January–March and October–December, with more than 2000 total time points exhibiting light pollution determined in this manner, consisting of approximately 23% of measurements made throughout 2020.

The *aurora borealis* was also detected in this manner, but was rarer and accounted for a much smaller proportion of the overall irradiance. Setting criteria of the E_G proportion being above 40% in the months of January–March and October–December (to make visual verification possible using the all-sky photographs), 250 instances of this condition were recorded throughout this period with the majority in February and October.

Additionally, the E_XSpec or E_X data can be combined with *in vivo* absorption spectra of photosynthetic organisms, in our case diatoms (using the mean values from six species of bloom forming diatoms characterized by Chl a, Chl c, and fucoxanthin as major light harvesting pigments), to provide estimates of AQ_{total} throughout the year making use of Eq. (5). Figure 12(A) shows the mean *in vivo* spectral absorption coefficient, ($a^*_\varphi(\lambda)$, green line) and the corresponding light utilized by photosystem II (PSII), ($F^*_{PSII}(\lambda)$, purple line, as presented in [21]. Using Eq. (5), AQ_{total} (using $a^*_\varphi(\lambda)$) and AQ_{PSII} (using $F^*_{PSII}(\lambda)$), indicating that ecologically relevant light absorption and utilization estimates across the year, can be calculated. Figure 12(B) shows both AQ_{total} and AQ_{PSII}, calculated using a spectroradiometer derived E_{PAR}Spec as the input in Eq. (5).

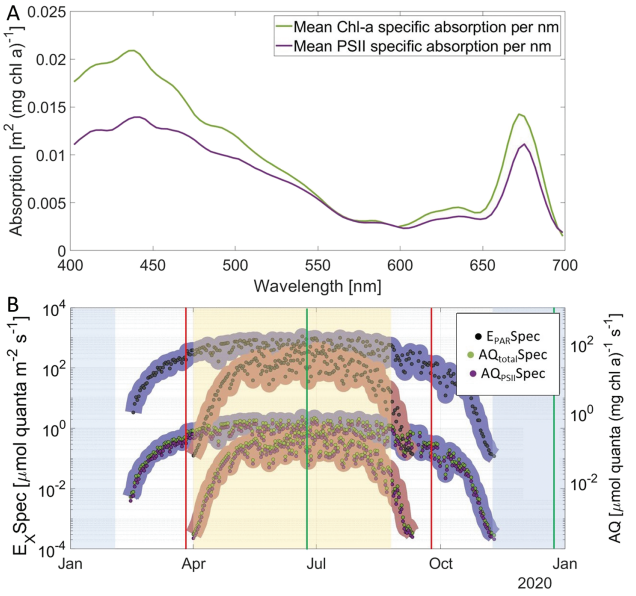

Fig. 12. A, *in vivo* spectrally light absorbed and fraction utilized by PSII of major primary producers (diatoms) and the corresponding E_{PAR}Spec in the Arctic through a whole annual cycle. A, mean Chl a-specific absorption coefficients of six of diatoms ($a^*_\varphi(\lambda)$, green line, total pigment absorption by cells) and the corresponding fraction of light utilized by PSII by using fluorescence excitation spectra ($F^*_{\mathrm{PSII}}(\lambda)$, purple line). B, annual absorbed and PSII utilized quanta in diatoms. Primary axis, E_XSpec providing spectrally resolved E_{PAR} measurements at noon (blue shading) and midnight (red shading); secondary axis, corresponding $\mathrm{AQ_{total}}$ (green dots) and $\mathrm{AQ_{PSII}}$ (purple dots) calculated using Eq. (5).

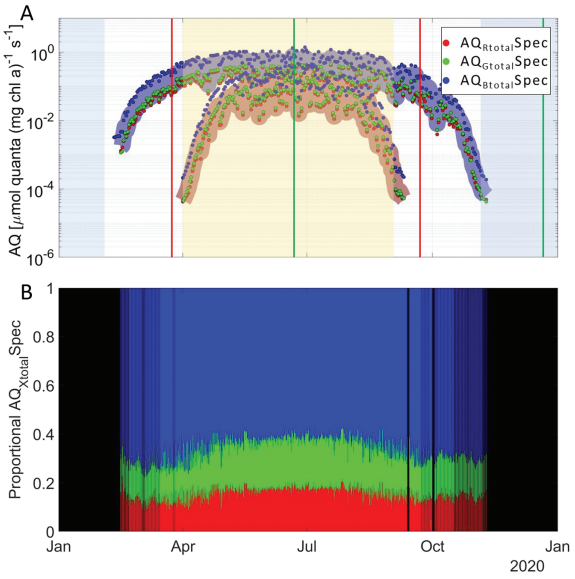

Fig. 13. A, AQ_{total} in three bands: 400–500 nm (blue), 500–600 nm (green), and 600–700 nm (red) using $a^*_\varphi(\lambda)$, and $E(\lambda)$ from the spectoradiometer in Eq. (5) (blue shading, noon measurements; red shading, midnight measurements). The background blue and yellow shaded areas denote the Polar Night and the Midnight Sun periods, while the red and green lines denote the equinox and solstices. B, proportions of the total absorbed light in each band.

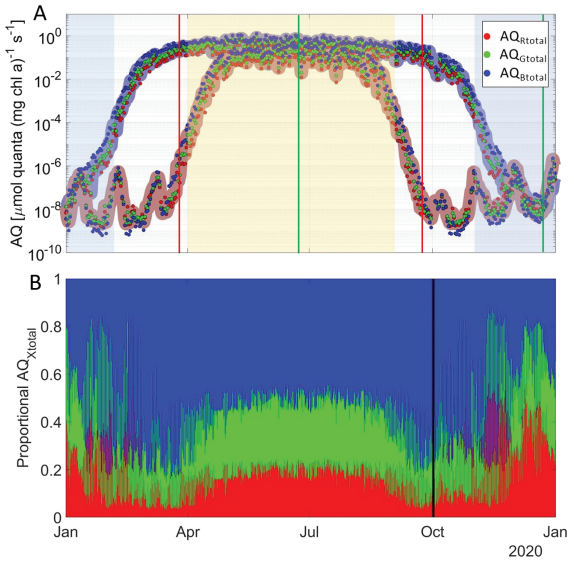

Fig. 14. A, AQ_{total} by diatoms in three color bands: Blue (412–555 nm), green (468–635 nm), and red (505–691 nm) using camera derived E_X irradiance data as input. The background blue and yellow shaded areas denote the Polar Night and the Midnight Sun periods, while the red lines denote the equinox, and the green lines denote solstices. B, proportions of the total AQ_{total} in each color channel.

As this information ($a^*_\varphi(\lambda)$, $F^*_{\mathrm{PSII}}(\lambda)$, and E_{PAR}Spec) is spectrally resolved, wavelength bands can be defined as required. For example, Fig. 13(A) shows $\mathrm{AQ_{total}}$ throughout the year with the following selected wavelength bands: red, 600–700 nm; green, 500–600 nm; and blue, 400–500 nm. Figure 13(B) shows the normalized proportion of $\mathrm{AQ_{total}}$ which is within each band. This indicates that of these spectral bands most of $\mathrm{AQ_{total}}$ lies within the 400–500 nm blue range. The information around the low light periods is again hard to obtain as it falls below the applied threshold of the spectroradiometer. The camera data again provide a method to address the lack of sensitivity of the spectroradiometer in the darkest periods.

As shown in [13], the camera's sensitivity as an irradiance sensor allows for additional information to be gleaned regarding the low light periods of the year. To make use of that additional sensitivity here, several steps must be taken. As noted previously, the camera data are not fully spectrally resolved but, by calculating an average absorption coefficient from the data in Fig. 12(A) for each color band, the AQ can be calculated in a similar manner to above but using the following wavebands: red, 505–691 nm; green, 468–635 nm; and blue, 412–555 nm, as outlined in Fig. 5(A). This is a less flexible method than using the spectroradiometer, but does allow for the AQ estimates during low light conditions such as night time or in the Polar Night, as shown in Fig. 14(A), when combined with E_X data from the camera as input to Eq. (5).

Here the range can be better seen in the spring and autumn transition periods and the dark periods of the year and give an indication of the dominant wavelength bands absorbed at different times of the day throughout the year. This shows that in the transition periods (spring and autumn periods of increasing and decreasing irradiance, respectively, centered on the equinoxes), the blue band, which makes up most of the AQ in the summer months, is replaced by increased amounts of red and green light

Table 1. Monthly Maximum, Minimum, Average, and Ratio of AQ_{Xtotal} for each Color Band (R, 505–691 nm; G, 468–635 nm; B, 412–555 nm) Derived from the Camera and Corresponding $a^*_\varphi(\lambda)$ for Diatoms[a]

	Max (*μmol quanta (mg Chl a)$^{-1}$ s^{-1}*)			Min (*μmol quanta (mg Chl a)$^{-1}$ s^{-1}*)		
2020	AQ_{Rtotal}	AQ_{Gtotal}	AQ_{Btotal}	AQ_{Rtotal}	AQ_{Gtotal}	AQ_{Btotal}
Jan	9.7E-06	7.8E-06	1.9E-05	1.4E-09	1.9E-09	5.8E-10
Feb	3.4E-02	6.7E-02	1.3E-01	1.7E-09	2.1E-09	6.9E-10
Mar	2.3E-01	3.3E-01	5.3E-01	3.5E-09	3.7E-09	2.5E-09
Apr	5.1E-01	6.5E-01	9.4E-01	3.3E-06	1.1E-05	5.4E-05
May	6.3E-01	8.3E-01	1.3E+00	1.6E-02	2.4E-02	4.1E-02
Jun	6.0E-01	7.8E-01	1.1E+00	1.2E-02	1.9E-02	3.4E-02
Jul	6.0E-01	7.6E-01	1.1E+00	7.1E-03	1.5E-02	3.3E-02
Aug	5.0E-01	6.4E-01	9.1E-01	1.0E-04	2.4E-04	7.2E-04
Sep	2.8E-01	3.7E-01	5.4E-01	4.2E-09	3.8E-09	1.5E-09
Oct	7.2E-02	1.0E-01	1.6E-01	1.6E-09	2.0E-09	6.6E-10
Nov	2.6E-04	6.2E-04	1.8E-03	6.7E-09	4.9E-09	1.8E-09
Dec	4.2E-06	5.7E-06	9.5E-06	7.6E-09	5.4E-09	2.5E-09
	Average (*μmol quanta (mg Chl a)$^{-1}$ s^{-1}*)			Ratio of daily max to daily min		
2020	AQ_{Rtotal}	AQ_{Gtotal}	AQ_{Btotal}	AQ_{Rtotal}	AQ_{Gtotal}	AQ_{Btotal}
Jan	1.1E-07	1.6E-07	4.6E-07	7153	4091	32138
Feb	1.1E-03	2.0E-03	4.4E-03	20478740	32314172	194856438
Mar	2.7E-02	4.3E-02	7.8E-02	67001776	87766044	212331735
Apr	1.1E-01	1.6E-01	2.7E-01	154407	57356	17353
May	1.9E-01	2.6E-01	4.1E-01	39	34	31
Jun	2.1E-01	2.9E-01	4.4E-01	50	40	33
Jul	1.8E-01	2.4E-01	3.7E-01	84	52	31
Aug	1.0E-01	1.5E-01	2.3E-01	5003	2673	1271
Sep	3.9E-02	5.6E-02	9.2E-02	67121027	98778925	369534162
Oct	3.0E-03	4.9E-03	9.1E-03	46046894	52309160	241584328
Nov	3.2E-06	7.4E-06	2.3E-05	38235	127561	999899
Dec	1.3E-07	1.4E-07	1.7E-07	553	1057	3863

[a]The red and green boxes denote the month within which the equinox and solstice dates occur, respectively; the gray shading is the Polar Night period, and the yellow shading is the Midnight Sun period.

creating a much more dynamic light environment for the local ecosystem. This is influenced by the local light climate which has a large level of artificial sources influencing skyglow during the darker periods. This should be considered when extrapolating to other areas where artificial light sources are less abundant.

Table 1 shows specific parameters relating to the AQ_{Xtotal} data shown in Fig. 14(A). The maximum, minimum, average, and dynamic range data per month in 2020 are shown. The dynamic range of the calculated AQ is a ratio of the maximum and minimum monthly values to illustrate the change in the monthly amplitude of AQ throughout the year. These data are shown in Fig. 15 below. The calculated AQ_{Btotal} values for the blue channel are highly dynamic in the Polar Night period due to weather impacts and the lunar cycle and during the transition months (spring and autumn equinox periods), while relatively stable across the Midnight Sun period, when both AQ_{Rtotal} and AQ_{Gtotal} show minimal amplitude variation.

To further illustrate the variability throughout the year when using AQ_{Xtotal} data from the camera-based system, a threshold of ecologically relevant irradiance and color bands can be applied. This gives information regarding light availability and as a cue for photosynthetic organisms at different seasons, including daily differences which, in turn, can provide an indication of which color sensitive photoreceptors (all organisms have color band-sensitive photoreceptors that induce gene expression for all physiological processes in a given organism,

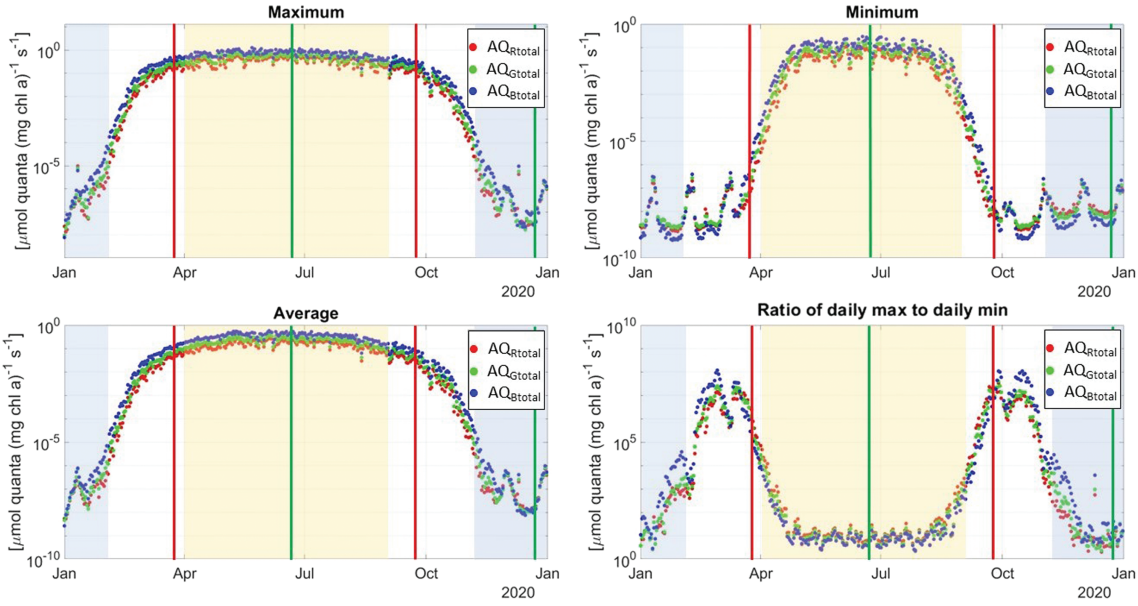

Fig. 15. Daily maximum, minimum, average, and corresponding ratios of daily maximum to daily minimum of AQ_{total} derived using $a^*_\varphi(\lambda)$ and $E_{R,G,B}$ derived from camera data.

Table 2. Calculated % of Hours per Month (H%) with AQ_{Xtotal} Above a Threshold Corresponding to Incident Irradiance of $E_X = 0.01$ μmol quanta m^{-2} s^{-1}[a]

	AQ_{Rtotal} H%	AQ_{Gtotal} H%	AQ_{Btotal} H%	Total Hours R	Total Hours G	Total Hours B
Jan	0.0	0.0	0.0	0	0	0
Feb	23.7	26.3	28.9	25	42	68
Mar	58.5	62.0	64.2	246	267	288
Apr	98.6	99.8	100.0	451	467	490
May	100.0	100.0	100.0	592	592	592
Jun	100.0	100.0	100.0	570	570	570
Jul	100.0	100.0	100.0	585	585	585
Aug	100.0	100.0	100.0	534	550	562
Sep	76.5	79.3	81.3	353	395	422
Oct	37.1	39.0	40.6	64	104	134
Nov	3.5	4.6	5.8	0	0	0
Dec	0.0	0.0	0.0	0	0	0

[a]Color coding as in Table 1. The total hours are approximate, as not all months have a complete unbroken time series.

as detailed in Valle *et al.* and Nymark *et al.* [14,24]) may be responding differently at different times of the year. As behavior and function are dictated by photoreceptors providing cues for gene expression of all cellular processes, the relative light levels between color bands throughout the year may influence organism behavior and activity [25,26].

Table 2 shows the calculated % of hours per month, where the AQ_{Xtotal} levels were above a theoretical incident irradiance threshold value for photosynthesis of $E_X =$ 0.01 μmol quanta m^{-2} s^{-1} [1] which was applied to all three color bands. The total number of hours measured as above threshold is also shown; note that not all months have a complete continuous time series. There appears to be little difference between the bands; however, in the Polar Night, there are brief periods where only AQ_{Btotal} is above the threshold while, in the Midnight Sun period, all bands are active. As noted in [14], "genes responsible for the repair of photodamaged PSII [are] strongly induced in blue light, intermediately expressed in green light and weakest induced in red light" and "green and red lights [are] the strongest inducers of LHC genes encoding antenna

proteins involved in light harvesting." This suggests that there are periods of the Polar Night, highly important in dark periods (i.e., night globally) where repair and maintenance functions are carried out by organisms in the absence of appreciable levels of red or green light and light harvesting does not take place.

The threshold level applied here is purely theoretical, being derived from the threshold for actinic (photosynthetic) activity; it is the E_{PAR} threshold for all wavelengths between 400 and 700 nm and not wavelength specific. Further analysis and experimentation with appropriate waveband specific threshold levels could provide a clearer picture of the ecological effects of temporally resolved light levels on organisms living in the polar regions and insight into light availability for RGB photoreceptor-mediated behavior and functions.

5. CONCLUSION

As shown in [13], the use of a camera system to measure irradiance can go a long way towards overcoming the sensitivity requirements to make measurements in the low light conditions in the Polar Night periods in the high Arctic and at nighttime (dark periods of day) elsewhere globally. Indeed, all-sky cameras are in use in numerous locations around the world monitoring aurora and weather conditions, making astronomical observations, measuring solar energy for renewable energy generation, etc., many employing similar techniques of irradiance estimation [27–33]. Additional techniques, including mechanical or digital sun tracking and blocking [34,35] and deep learning for forecasting [36,37], are also in use. Few observatories are focused on the same ecological impacts as the ArcLight observatory. However, the simple postprocessing techniques used can be applied to images captured by most all-sky observatories with very little modification, meaning that this method can potentially be applied worldwide with datasets from many observatories and spectral responses from ecologically appropriate organisms/systems. While not fully spectrally resolved, the increase in sensitivity granted by the camera system can be taken advantage of to provide information in broad spectral bands corresponding to the RGB channels of the camera system, even in extreme low light during the Polar Night.

Having an image collected at each time point also provides the advantage of marrying spectral information to direct observation of environmental conditions at the time of a measurement, allowing for categorization of observations that may be of particular interest, i.e., aurora or anthropogenic light pollution, biologically defined day-length, and precipitation (e.g., snow on dome). The images also include information which is not detected by other instruments, i.e., lights on the horizon which are not detected by cosine corrected irradiance sensors.

The RGB channels of the camera are broadly similar to the photoreceptors in many biological systems; as such, the RGB data extracted from the all-sky camera can be used as inputs for ecological models along the lines of the absorbed quanta calculations for diatoms included in Section 4. Additionally, the ability to provide partial spectral discrimination into broad wavebands, even during the darkest periods (whether during the Polar Night or indeed dark night time periods anywhere), can provide a useful comparison for verification of theoretical light field models and provide realistic ecologically relevant inputs for underwater light field modeling in both the Arctic region and globally.

Funding. Norges Forskningsråd (223254, 245923, 276730, 300333); Natural Environment Research Council (NE/P00573X/1).

Acknowledgment. The authors would like to thank researchers at the Norwegian Polar Institute and Kings Bay in Ny-Ålesund for their logistical help. They also thank Pedro De La Torre and Sturla Haltbakk (NTNU) for their assistance in building the ArcLight observatory, and Tomasz Kopec (UiT–The Arctic University of Norway) for assistance with data handling and access.

Disclosures. The authors declare no conflicts of interest.

Data availability. All data used in the present study will be fully open access through the National Infrastructure for Research Data (NIRD). The data are published in datasets covering an annual time series (2017–2020 available, only 2020 used in this work) from the spectroradiometer (raw data and E_{PAR} data [38,39]) and from an all-sky camera (images and E_{PAR} data [40,41]).

REFERENCES

1. J. Berge, M. Daase, P. E. Renaud, *et al.*, "Unexpected levels of biological activity during the polar night offer new perspectives on a warming arctic," Curr. Biol. **25**, 2555–2561 (2015).
2. K. S. Last, L. Hobbs, J. Berge, A. S. Brierley, and F. Cottier, "Moonlight drives ocean-scale mass vertical migration of zooplankton during the Arctic winter," Curr. Biol. **26**, 244–251 (2016).
3. J. H. Cohen, J. Berge, M. A. Moline, A. J. Sørensen, K. Last, S. Falk-Petersen, P. E. Renaud, E. S. Leu, J. Grenvald, F. Cottier, H. Cronin, S. Menze, P. Norgren, Ø. Varpe, M. Daase, G. Darnis, and G. Johnsen, "Is ambient light during the high Arctic polar night sufficient to act as a visual cue for zooplankton?" PloS One **10**, e0126247 (2015).
4. M. Ludvigsen, J. Berge, M. Geoffroy, J. H. Cohen, P. R. de La Torre, S. M. Nornes, H. Singh, A. J. Sørensen, M. Daase, and G. Johnsen, "Use of an autonomous surface vehicle reveals small-scale diel vertical migrations of zooplankton and susceptibility to light pollution under low solar irradiance," Sci. Adv. **4**, eaap9887 (2018).
5. J. Berge, P. E. Renaud, G. Darnis, F. Cottier, K. Last, T. M. Gabrielsen, G. Johnsen, L. Seuthe, J. M. Weslawski, E. Leu, M. Moline, J. Nahrgang, J. E. Søreide, Ø. Varpe, O. J. Lønne, M. Daase, and S. Falk-Petersen, "In the dark: a review of ecosystem processes during the Arctic polar night," Prog. Oceanogr. **139**, 258–271 (2015).
6. J. Berge, G. Johnsen, and J. H. Cohen, "Introduction," in *POLAR NIGHT Marine Ecology: Life and Light in the Dead of Night* (Springer, 2020), pp. 1–16.
7. H. A. Cronin, J. H. Cohen, J. Berge, G. Johnsen, and M. A. Moline, "Bioluminescence as an ecological factor during high Arctic polar night," Sci. Rep. **6**, 36374 (2016).
8. G. Johnsen, M. Candeloro, J. Berge, and M. Moline, "Glowing in the dark: discriminating patterns of bioluminescence from different taxa during the Arctic polar night," Polar Biol. **37**, 707–713 (2014).
9. J. Berge, M. Daase, L. Hobbs, S. Falk-Petersen, D. Gerald, and J. Søreide, "Zooplankton in the polar night," in *POLAR NIGHT Marine Ecology: Life and Light in the Dead of Night*, .J. Berge, G. Johnsen, and J. H. Cohen, eds. (Springer, 2020), pp. 113–116.
10. G. Johnsen, E. Leu, and R. Gradinger, "Marine micro- and macroalgae in the polar night," in *POLAR NIGHT Marine Ecology: Life and Light in the Dead of Night*, J. Berge, G. Johnsen, and J. H. Cohen, eds. (Springer, 2020) pp. 67–112.
11. J. H. Cohen, K. S. Last, C. L. Charpentier, F. Cottier, M. Daase, L. Hobbs, G. Johnsen, and J. Berge, "Photophysiological cycles in Arctic krill are entrained by weak midday twilight during the Polar Night," PloS Biol. **19**, e3001413 (2021).
12. J. H. Cohen, J. Berge, M. A. Moline, G. Johnsen, and A. P. Zolich, "Light in the Polar Night," in *POLAR NIGHT Marine Ecology: Life and Light in the Dead of Night*, J. Berge, G. Johnsen, and J. H. Cohen, eds. (Springer, 2020) pp. 37–66.

13. G. Johnsen, A. Zolich, S. Grant, R. Bjørgum, J. H. Cohen, D. McKee, T. P. Kopec, D. Vogedes, and J. Berge, "All-sky camera system providing high temporal resolution annual time series of irradiance in the Arctic," Appl. Opt. **60**, 6456–6468 (2021).
14. K. C. Valle, M. Nymark, I. Aamot, K. Hancke, P. Winge, K. Andresen, G. Johnsen, T. Brembu, and A. M. Bones, "System responses to equal doses of photosynthetically usable radiation of blue, green, and red light in the marine diatom phaeodactylum tricornutum," PloS One **9**, e114211 (2014).
15. International Electrotechnical Commission, "Multimedia systems and equipment–Color measurement and management–Part 2-1: Color management–Default RGB color space–sRGB," IEC 61966-2-1 (1999).
16. P. D. Hiscocks, *Measuring Luminance with a Digital Camera* (Syscomp Electronic Design, 2014).
17. "Photography—General purpose photographic exposure meters (photoelectric type)—Guide to product specification," (1974).
18. R. Kawakami, H. Zhao, R. T. Tan, and K. Ikeuchi, "Camera spectral sensitivity and white balance estimation from sky images," Int. J. Comput. Vis. **105**, 187–204 (2013).
19. G. Johnsen, E. Sakshaug, and M. Vernet, "Pigment composition, spectral characterization and photosynthetic parameters in Chrysochromulina polylepis," Mar. Ecol. Prog. Ser. **83**, 241–249 (1992).
20. S. Connan-McGinty, N. S. Banas, J. Berge, F. Cottier, S. Grant, G. Johnsen, T. P. Kopec, M. Porter, and D. McKee, "Midnight Sun to Polar Night: a model of seasonal light in the Barents sea," J. Adv. Model Earth Syst. **14**, e2022MS003198 (2022).
21. E. Sakshaug, G. Johnsen, S. Kristiansen, C. Quillfeldt, C. Von, F. Rey, D. Slagstad, and F. Thingstad, "Phytoplankton and primary production," in *Ecosystem Barents Sea*E. Sakshaug, G. Johnsen, and K. Kovacs, eds. (Tapir Academic Press, 2009), pp. 167–208.
22. A. Roesch and H. Schmidbauer, "WaveletComp: computational wavelet analysis," (2018).
23. J. Berge, M. Geoffroy, M. Daase, F. Cottier, P. Priou, J. H. Cohen, G. Johnsen, D. McKee, I. Kostakis, P. E. Renaud, D. Vogedes, P. Anderson, K. S. Last, and S. Gauthier, "Artificial light during the polar night disrupts Arctic fish and zooplankton behaviour down to 200 m depth," Commun. Biol. **3**, 102 (2020).
24. M. Nymark, K. C. Valle, T. Brembu, K. Hancke, P. Winge, K. Andresen, G. Johnsen, and A. M. Bones, "An integrated analysis of molecular acclimation to high light in the marine diatom Phaeodactylum tricornutum," PloS One **4**, e114211 (2009).
25. V. B. Veedin Rajan, N. S. Häfker, E. Arboleda, B. Poehn, T. Gossenreiter, E. Gerrard, M. Hofbauer, C. Mühlestein, A. Bileck, C. Gerner, M. Ribera d'Alcala, M. C. Buia, M. Hartl, R. J. Lucas, and K. Tessmar-Raible, "Seasonal variation in UVA light drives hormonal and behavioural changes in a marine annelid via a ciliary opsin," Nat. Ecol. Evol. **5**, 204–218 (2021).
26. N. S. Häfker, S. Connan-McGinty, L. Hobbs, D. McKee, J. H. Cohen, and K. S. Last, "Animal behavior is central in shaping the realized diel light niche," Commun. Biol. **5**, 562 (2022).
27. F. Sigernes, M. Syrjäsuo, B. Lybekk, E. Trondsen, L. Clausen, M. Kellinsalmi, J. Mattanen, K. Kauristie, C. Hall, and M. G. Johnsen, [BACC: THE BOREAL AURORAL CAMERA CONSTELLATION] The Boreal Aurora Camera Constellation (BACC)-Status 2023 (2023).
28. E. Ntavelis, J. Remund, and P. Schmid, "SkyCam: a dataset of sky images and their irradiance values" (2021).
29. P. C. Valdelomar, J. L. Gómez-Amo, C. Peris-Ferrús, F. Scarlatti, and M. P. Utrillas, "Feasibility of ground-based sky-camera HDR imagery to determine solar irradiance and sky radiance over different geometries and sky conditions," Remote Sens. **13**, 5157 (2021).
30. Y. Chu, M. Li, H. T. C. Pedro, and C. F. M. Coimbra, "A network of sky imagers for spatial solar irradiance assessment," Renew Energy **187**, 1009–1019 (2022).
31. S. Dev, F. M. Savoy, Y. H. Lee, and S. Winkler, "Estimating solar irradiance using sky imagers," Atmos. Meas. Tech. **12**, 5417–5429 (2019).
32. J. Alonso-Montesinos and F. J. Batlles, "The use of a sky camera for solar radiation estimation based on digital image processing," Energy **90**, 377–386 (2015).
33. B. Kurtz and J. Kleissl, "Measuring diffuse, direct, and global irradiance using a sky imager," Solar Energy **141**, 311–322 (2017).
34. R. Mondragón, J. Alonso-Montesinos, D. Riveros-Rosas, M. Valdés, H. Estévez, A. E. González-Cabrera, and W. Stremme, "Attenuation factor estimation of direct normal irradiance combining sky camera images and mathematical models in an inter-tropical area," Remote Sens. **12**, 1212 (2020).
35. C. A. Gueymard, J. M. Bright, D. Lingfors, A. Habte, and M. Sengupta, "A posteriori clear-sky identification methods in solar irradiance time series: review and preliminary validation using sky imagers," Renew. Sustain. Energy Rev. **109**, 412–427 (2019).
36. S. Song, Z. Yang, H. H. Goh, Q. Huang, and G. Li, "A novel sky image-based solar irradiance nowcasting model with convolutional block attention mechanism," Energy Rep. **8**, 125–132 (2022).
37. T. A. Siddiqui, S. Bharadwaj, and S. Kalyanaraman, "A deep learning approach to solar-irradiance forecasting in sky-videos," in *IEEE Winter Conference on Applications of Computer Vision (WACV)* (Institute of Electrical and Electronics Engineers, 2019), pp. 2166–2174.
38. J. Berge, S. Grant, R. Bjørgum, J. H. Cohen, D. McKee, G. Johnsen, A. Zolich, T. P. Kopec, and D. L. Vogedes, "USSIMO spectroradiometer raw data time series (2020) measured under the dome of a light observatory in the Arctic (Ny-Ålesund, Svalbard, Norway)," NIRD Research Data Archive, 2021, https://doi.org/10.11582/2021.00046.
39. J. Berge, S. Grant, R. Bjørgum, J. H. Cohen, D. McKee, G. Johnsen, A. Zolich, T. K. Kopec, and D. L. Vogedes, "Time series (2020) of irradiance in the PAR (Photosynthetic Active Radiation) measured under the Dome of a light observatory in the Arctic (Ny-Ålesund, Svalbard, Norway) derived from an USSIMO spectroradiometer," NIRD Research Data Archive, 2021, https://doi.org/10.11582/2021.00050.
40. G. Johnsen, S. Grant, R. Bjørgum, J. H. Cohen, D. McKee, T. P. Kopec, D. L. Vogedes, J. Berge, and A. Zolich, "Pictures from an all-sky camera with hourly resolution from the light observatory at Ny-Ålesund, Svalbard, Norway (complete year 2020)," NIRD Research Data Archive, 2021, https://doi.org/10.11582/2021.00021.
41. G. Johnsen, S. Grant, R. Bjørgum, J. H. Cohen, D. McKee, T. P. Kopec, D. L. Vogedes, J. Berge, and A. Zolich, "Time series (2020) of irradiance in the PAR (photosynthetically active radiation) region measured under the dome of a light observatory in the Arctic (Ny-Ålesund, Svalbard, Norway) derived from SLR camera," NIRD Research Data Archive, 2021, https://doi.org/10.11582/2021.00050.